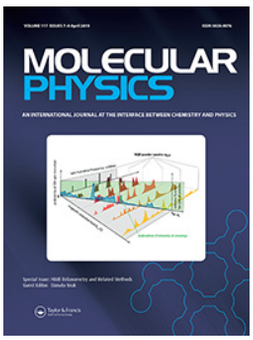

Taylor & Francis
Taylor & Francis Group

Molecular Physics

An International Journal at the Interface Between Chemistry and Physics

ISSN: 0026-8976 (Print) 1362-3028 (Online) Journal homepage: https://www.tandfonline.com/loi/tmph20

Comparison of fast field-cycling magnetic resonance imaging methods and future perspectives

Markus Bödenler, Ludovic de Rochefort, P. James Ross, Nicolas Chanet, Geneviève Guillot, Gareth R. Davies, Christian Gösweiner, Hermann Scharfetter, David J. Lurie & Lionel M. Broche

To cite this article: Markus Bödenler, Ludovic de Rochefort, P. James Ross, Nicolas Chanet, Geneviève Guillot, Gareth R. Davies, Christian Gösweiner, Hermann Scharfetter, David J. Lurie & Lionel M. Broche (2019) Comparison of fast field-cycling magnetic resonance imaging methods and future perspectives, Molecular Physics, 117:7-8, 832-848, DOI: 10.1080/00268976.2018.1557349

To link to this article: https://doi.org/10.1080/00268976.2018.1557349

Published online: 18 Dec 2018.

MOLECULAR PHYSICS
2019, VOL. 117, NOS. 7–8, 832–848
https://doi.org/10.1080/00268976.2018.1557349

Taylor & Francis
Taylor & Francis Group

NMR RELAXOMETRY AND RELATED METHODS

OPEN ACCESS Check for updates

Comparison of fast field-cycling magnetic resonance imaging methods and future perspectives

Markus Bödenler[a*], Ludovic de Rochefort[b*], P. James Ross[c], Nicolas Chanet[d], Geneviève Guillot[d], Gareth R. Davies[c], Christian Gösweiner [a], Hermann Scharfetter[a], David J. Lurie[c] and Lionel M. Broche[c*]

[a]Institute of Medical Engineering, Graz University of Technology, Graz, Austria; [b]CNRS, Center for Magnetic Resonance in Biology and Medicine (CRMBM) UMR 7339, Aix Marseille Univ, Marseille, France; [c]Aberdeen Biomedical Imaging Centre, University of Aberdeen, Aberdeen, UK; [d]Imagerie par Résonance Magnétique Médicale et Multi-Modalités, IR4M UMR 8081, Université Paris Saclay, Orsay, France

ABSTRACT

Fast field-cycling (FFC) nuclear magnetic resonance relaxometry is a well-established method to determine the relaxation rates as a function of magnetic field strength. This so-called nuclear magnetic relaxation dispersion gives insight into the underlying molecular dynamics of a wide range of complex systems and has gained interest especially in the characterisation of biological tissues and diseases. The combination of FFC techniques with magnetic resonance imaging (MRI) offers a high potential for new types of image contrast more specific to pathological molecular dynamics. This article reviews the progress in FFC-MRI over the last decade and gives an overview of the hardware systems currently in operation. We discuss limitations and error correction strategies specific to FFC-MRI such as field stability and homogeneity, signal-to-noise ratio, eddy currents and acquisition time. We also report potential applications with impact in biology and medicine. Finally, we discuss the challenges and future applications in transferring the underlying molecular dynamics into novel types of image contrast by exploiting the dispersive properties of biological tissue or MRI contrast agents.

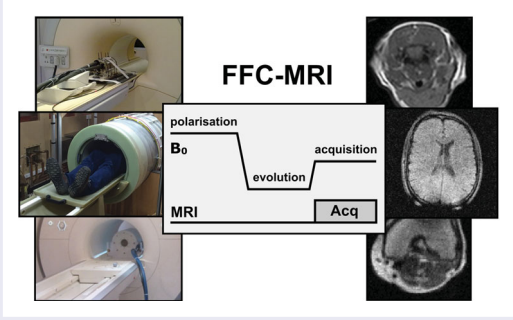

ARTICLE HISTORY
Received 29 June 2018
Accepted 30 November 2018

KEYWORDS
Field-cycling; FFC-MRI; delta relaxation enhanced MR; dispersion; NMRD

Introduction

Magnetic Resonance Imaging (MRI) has emerged as one of the most versatile imaging modalities in clinical diagnosis, providing a wealth of contrast mechanisms. In this respect, human (clinical) and animal (pre-clinical) MRI scans typically exploit differences in local proton (^{1}H) density (mostly tissue water content) and spatially varying longitudinal (T_1) and transverse (T_2 and T_2*) relaxation times or equivalently of their inverse, referred to as the relaxation rates R_1 and R_2 (and R_2*), respectively, measured at the fixed imaging magnetic field B_0 of the scanner. Differences in the underlying relaxation behaviour at B_0, and therefore changes in image contrast, can be used to distinguish between healthy and pathological tissues for many diseases [1]. However, contrast mechanisms may change dramatically with the applied magnetic field strength, and these changes can be exploited to obtain new information for medical diagnosis. One way to access field-dependant information is by using Fast Field-Cycling (FFC) methods.

FFC Nuclear Magnetic Resonance (NMR) relaxometry is an established method to measure the changes

CONTACT Markus Bödenler m.boedenler@tugraz.at
*These authors have equally contributed to this work.

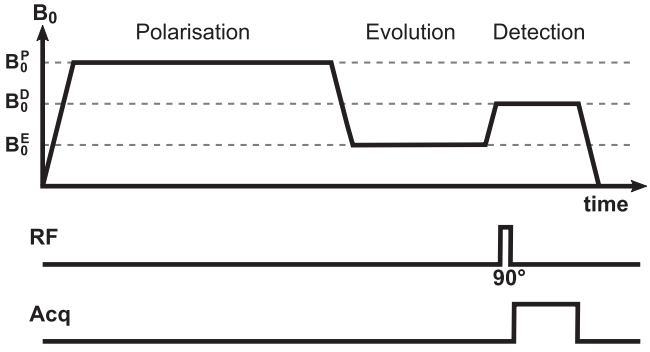

Figure 1. Example of a typical pulse sequence for FFC-NMR. The top line represents the main magnetic field, switching from 0 to polarisation B_0^P and evolution B_0^E followed by a transition to the detection field B_0^D. At the bottom the radiofrequency pulse and signal acquisition timing. Note that the transitions between the plateaus are much shorter than the typical T_1 values, a necessary condition for FFC-NMR.

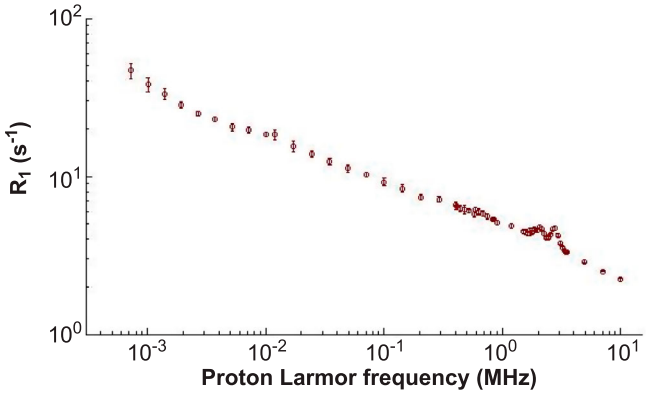

Figure 2. ^{1}H R_1 NMRD profile of healthy human cartilage obtained from the Aberdeen FFC-MRI research group [10]. Cartilage shows a marked dispersion over several decades of field strength, or equivalently proton Larmor frequency. Quadrupole peaks can also be observed around 2.5 MHz that inform on water–protein interactions.

of relaxation times with the field strength B_0, referred to as Nuclear Magnetic Relaxation Dispersion (NMRD) profiles. The magnetic field strength is typically rapidly cycled during the FFC-NMR experiment, allowing relaxation to occur at a wide range of field strengths but always returning to the same magnetic field for detection of NMR signals [2]. As an example Figure 1 shows a FFC-NMR pulse sequence. B_0 varies over time to form three plateaus: the first one is for polarisation and increases the amplitude of the signal response, the second plateau leaves the spin system to evolve at the field of interest with its corresponding T_1 value and the last plateau serves for detection of the ^{1}H NMR signal.

Repeating this sequence with different evolution times allows finding T_1 at the evolution field, so that repeating the overall method for different evolution fields provides a measurement of the dispersion of R_1 (an example of a ^{1}H R_1 NMRD profile is shown on Figure 2). As R_1 relaxation mostly depends on characteristic times of microscopic motions (such as translation and rotation) and possible energy dissipation through matching energy levels of some molecular structures (such as interactions with quadrupole nuclei), R_1 NMRD profiles give insight into the molecular dynamics and structural order of a wide range of complex systems such as organic solids, metals, polymers, liquid crystals, porous media, exogenous contrasts agents or biological systems [3–6]. While used for a long time as a tool in the development phases of MRI contrast agents, over the last decade FFC-NMR has gained interest in the characterisation of biological tissues and diseases [7–10] by either exploiting the endogenous ^{1}H R_1 NMRD profile itself, or its modifications produced by exogenous contrast agents. These results demonstrate that FFC methods have a great potential in medicine if combined with MRI and much efforts are dedicated to create FFC-MRI scanners [11–15].

Fast field-cycling adds an extra dimension to MRI by allowing the B_0 field to be changed during the pulse sequence and an optimal magnetic field can be selected for each of the main phases of an MRI pulse sequence (polarisation, relaxation and acquisition). This allows the generation of images displaying the variation of R_1 with respect to the magnetic field in *ex vivo* and *in vivo* biological tissues, non-invasively, with a high potential to generate new types of image contrast specific to pathological molecular dynamics and thus useful for disease characterisation and diagnosis.

Compared with conventional MRI, FFC-MRI requires dedicated hardware to vary the magnetic field B_0 rapidly compared to the relaxation times. Implementation poses strong constraints on magnet design, power supplies, control electronics, pulse sequences, scan time and image quality. These constraints require compromises and add serious difficulties to the construction of FFC-MRI scanners so that at present FFC-MRI system developments are limited only to a small number of research groups worldwide exploring different approaches ranging from completely home-built human-scale systems at low field to B_0 insert coils for commercial MRI systems at clinical fields of 1.5 T and 3 T.

The purpose of this article is to provide an overview of the recent advances in the field of FFC-MRI and to review different approaches as well as to present their advantages and drawbacks. First we present an overview of FFC-MRI hardware designs, their limitations and the error correction strategies being employed. Then we present the acquisition strategies currently developed to tackle

image reconstruction problems that are specific to FFC-MRI. Finally, we discuss the challenges and the potential applications that can arise by exploiting the dispersive properties of biological tissues and selected MRI contrast agents, transferring the underlying molecular dynamics into new types of image contrast on biological tissues, including living materials.

FFC-MRI technologies

Various systems exist that allow changing the magnetic field during a pulse sequence in an FFC-MRI system. Each technology presents its strengths and weaknesses. An overview of the early developments and history of FFC-MRI hardware systems can be found in references [11,16] and a summary of the latest hardware systems is presented in Table 1 and detailed below. Performing FFC-MRI systems are expected: (i) to switch the main magnetic field in a time shorter than the sample T_1 at these fields, (ii) to access a large range of magnetic field strength in order to provide a large overview of the R_1 NMRD profile, both at the high and low end of the Larmor frequency spectrum and (iii) to be large enough to accommodate relevant objects for imaging.

The practical implementation of these requirements necessitate to make various compromises and several designs exist that suit different purposes. FFC-MRI bears resemblance with ultra-low field MRI [17], which is not covered here, that similarly relies on electromagnets to produce a pre-polarising field but signal detection is performed with SQUIDs (Superconducting Quantum Interference Device) at the ultra-low field. Below is a description of the magnet technologies currently used for FFC-MRI.

Dual resistive and permanent whole-body magnets

This technology combines the stability of a permanent magnet with the reactivity of a resistive one, both of whole-body sizes. This approach has been developed in Aberdeen, UK [18,21] and can reach magnetic fields from 5 to 120 mT with an acquisition field of 59 mT. It consists of a vertical-field ferrite magnet using a Halbach configuration and a vertical resistive insert magnet that adds to or subtracts from the permanent field. The overall system has a bore size of 52 cm, which is enough for whole-body human scans.

A key element of the dual-magnet approach is that signal acquisition takes place only in the field of the permanent magnet, with the insert magnet inactivated, and the scanner exploits the short-term stability of the permanent magnet to avoid artefacts in the image, while the resistive magnet varies the relaxation field over a relatively large Larmor frequency range during the spin preparation stage. One drawback of this design is that the field inhomogeneities of the two magnets add up when reaching very low B_0 so that the lowest field attainable is about 1 mT when scanning an object the size of a head. Moreover, the use of ferrite magnets restricts the imaging field to relatively weak B_0, which limits polarisation (120 mT in the Aberdeen dual-magnet system) and increases the scan time required to obtain exploitable images. Additionally, the magnetic field generated by permanent magnets is temperature-dependant (on the order of 0.2% per degree for ferrite [18]), requiring either to control the room air temperature or to monitor the variations of the magnetic field.

Single resistive magnet

FFC-MRI designs based on a single resistive magnet present two main advantages: they can produce relatively strong magnetic fields per weight compared with a permanent magnet and the homogeneity of the magnet scales with the current so that it is not the dominant limitation when reaching very low magnetic fields. Current developments focus on a completely resistive whole-body FFC-MRI device [19] in an effort to reach even lower B_0 fields for relaxation on the one hand and to increase the imaging field strength on the other hand. This scanner has a bore of 50 cm, which is quite narrow but does permit whole-body scans of slim people (see Figure 3(a)). It is capable of reaching field strengths up to 0.2 T and down to 100 µT but work is currently in progress to extend its lower limit to 5 µT to extend the range of the NMRD profile. The use of a purely resistive magnet makes it easier to explore low magnetic fields because the magnet inhomogeneities scale down with the field strength so that the limitations in the ultra-low field regime mainly come from the Earth's field (typically 40 µT depending on the location) and from magnetic fluctuations from the environment, such as moving elevators, nearby traffic, mains electricity supply or ferromagnetic structures within the building. The latter may generate local fields significantly stronger than Earth's as well as field gradients (10–50 µT/m is not uncommon). However, FFC experimentation imposes fast current variations in the magnet so that its inductance must be kept to a minimum. Low inductance makes it more difficult to drive the magnet consistently and limits the field stability so that particularly stable and fast current amplifiers are required for this scanner.

Superconducting magnet with resistive insert coil

Alternatively, FFC-MRI can be implemented by inserting a resistive B_0 insert coil into an otherwise conventional

clinical MRI system (see Figure 3(b)). The resistive B_0 insert coil provides the B_0 field modulations necessary for field-cycling experiments while images can be acquired by the MRI system as usual. This combines the advantage of a stable acquisition field, provided by the permanent or superconducting primary magnet of a conventional MRI system, with the fast-switching capability of a resistive coil with low inductance. The offset coil can be mounted on the patient table and positioned at the isocenter of the main magnet. The insertion coil is designed for an easy installation and removal, and provides a flexible utilisation of the FFC technology, while maintaining the basic operation mode of the MRI system. A schematic of a typical on-site integration can be found in Figure 3(c).

Several research groups worldwide have realised this approach, employing magnetic field strengths used in current clinical routine such as 1.5 T and 3 T, in order to implement a method known as delta relaxation enhanced magnetic resonance (dreMR) imaging, aimed at exploiting the detection of molecules (including contrast agents) with particular dispersion characteristics. Alford et al. [22] at the University of Western Ontario were the first

Table 1. Overview of current FFC-MRI systems and their characteristics.

FFC-MRI system	Type	Acquisition field	FFC range	Bore size
Bödenler et al. [15]	Insert coil	2.89 T	2.79–2.99 T	Small animal
de Rochefort et al. [14]	Insert coil	1.5 T	1–2 T	Small animal
Harris et al. [12]	Insert coil	1.5 T	1.28–1.72 T	Small animal
Hoelscher et al. [13]	Insert coil	1.5 T	1.41–1.59 T	Small animal
Lurie et al. [18]	Dual resistive and permanent	59 mT	5–120 mT	Whole-body
Ross et al. [19]	Resistive	0.2 T	0.1 mT–0.2 T	Whole-body
Pine et al. [20]	Insert coil	59 mT	3–115 mT	Forearm

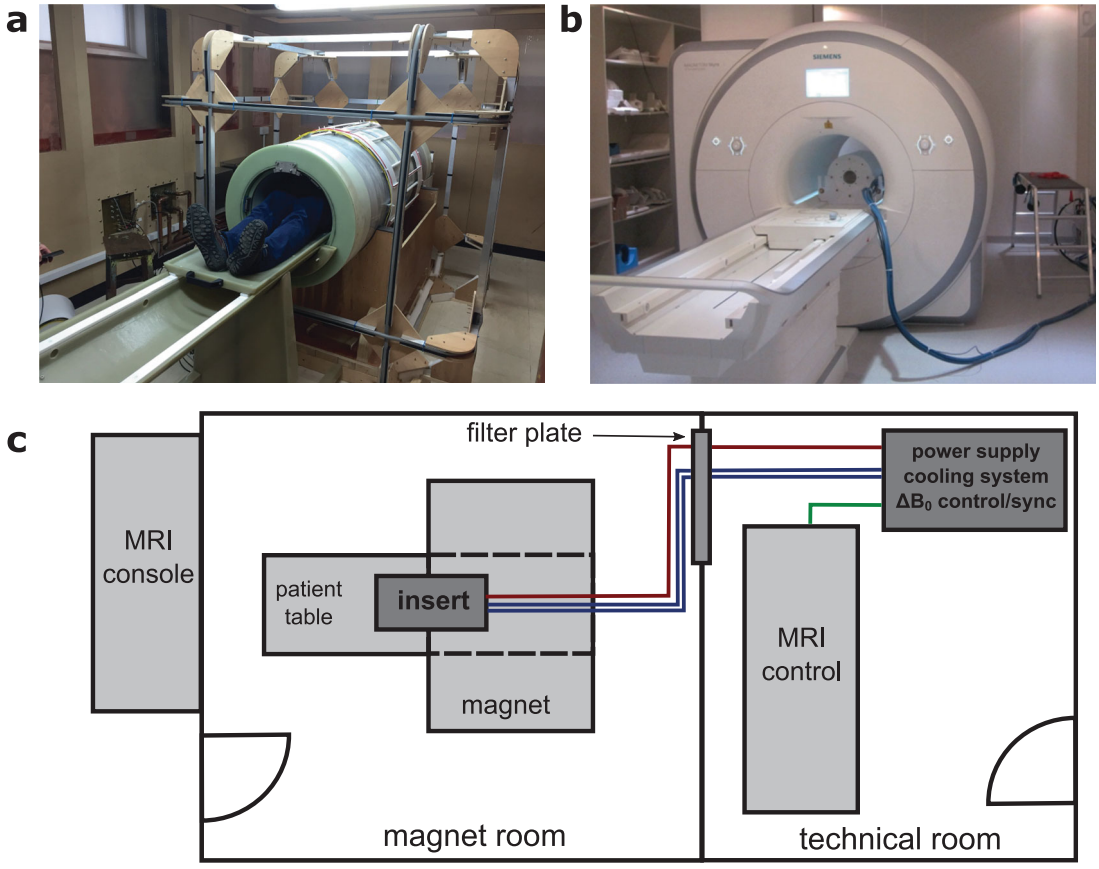

Figure 3. Integration of the FFC-MRI systems in their respective environments. (a) Current developments at the University of Aberdeen focus on a completely resistive human-scale FFC-MRI device [19] reaching a field strength up to 0.2 T. This scanner has a bore of 50 cm allowing for whole-body scans of slim people. (b) Shows a resistive B_0 insert coil within the bore of a superconducting magnet system at a field strength of 3 T [15]. Although this method uses clinical MRI systems for signal detection, the small bore sizes limit the imaging volume to pre-clinical small animal experiments. (c) Schematic of a typical on-site integration of an insert coil for an otherwise commercial MRI system.

Table 2. Comparison of B_0 insert coil specifications.

					Imaging region		Physical dimensions			
dreMR coil	ΔB_0 (mT)	L (mH)	R (mΩ)	Field efficiency (mT/A)	Ø (mm)	Length (mm)	Bore Ø (mm)	Outer Ø (mm)	Length (mm)	Theoretical power at max. field
Hoelscher et al. [13]	±90	4.90	60	2.54	34	50	52	242	340	75 W
Harris et al. [12]	±220	1.46	95	0.87	25	50	80	320	420	6.1 kW
de Rochefort et al. [14]	±500	0.30	100	1.57	28	40	40	170	300	10 kW
Bödenler et al. [15]	±100	1.69	64	0.67	40	40	100	345	514	1.4 kW

to describe the use of an insert coil, capable of modest field shifts of ±70 mT, within a clinical MRI system with a nominal field strength of 1.5 T. Later on, this first prototype insert coil design was improved by Harris et al. [12] leading to B_0 offset fields of ±0.22 T. Other systems at 1.5 T were implemented by Hoelscher et al. [13] and de Rochefort et al. [14], the latter reporting the currently highest ΔB_0 of ±0.5 T. Although the majority of available hardware setups are based on 1.5 T MRI systems, recently, Bödenler et al. [15] proposed an implementation centred at a nominal B_0 field strength of 2.89 T. Table 2 compares hardware specifications like ΔB_0, inductance, resistance, field efficiency, imaging region and physical dimensions of B_0 insert coils currently used for dreMR.

Despite the use of a clinical MRI system for signal detection, the bore sizes of all these insert coils are small (ranging from 40 to 100 mm in diameter). The limitation mostly comes from the inductive coupling between the resistive insert and the superconducting magnet: large currents are used in the resistive coil to generate large magnetic fields that are switched quickly, so the large variations of the insert stray field induce electric currents in the conductive parts of the permanent magnet. These currents may quench it during the B_0 field ramps. One way to mitigate this problem is to use an active shield to minimise the interaction with the host system. Another way is to reduce the size of the insert coil: the stray field decreases with the cube of the diameter to distance ratio so that smaller inserts produce a weaker stray field in the scanner structure and allow maintaining fast ramps. However, they offer a small imaging volume (ranging from 25 to 40 mm in diameter) that limits the use of such systems to pre-clinical small animal experiments. Yet feasibility studies by Harris et al. [23,24] have investigated B_0 insert coil designs suitable for human head and prostate imaging, which is an important step for transferring the dreMR method to human-scale applications.

Another important consideration is the power deposited in such an insert coil as it scales with the square of the required current and therefore field strength. Considering the designs presented in Table 2, it can be estimated that the power dissipated by Joule effects at maximum fields ranges between 75 W to 10 kW. An adapted cooling system is then required for heat extraction from the resistive windings for each system. Limited cooling capacity of the insert coil requires duty cycle adjustments or/and the maximum field (current) must be reduced. Therefore, a sufficient cooling capacity of the insert coil has to be considered during the design process as a change after construction is difficult. For example, the insert coil from Hoelscher et al. is limited to a duty cycle of 1:8 to allow for sufficient cooling. Harris et al. [12] implemented an effective cooling system so that the operation (6 kW generated at maximum field) is only limited by the duty-cycle of the power supply. They utilise a parallel water flow through each winding layer to increase the water flow and therefore the heat extraction. The cooling system involved in [14] (10 kW generated at maximum field) has a primary closed-loop circuit with circulating perfluorocarbon in contact with the insert coil and a secondary circuit with circulating water. The insert coil (1.4 kW at maximum field) in [15] employs a cooling system with six internal multipath circuits filled with water and the operation is only limited by the duty cycle of the power supply.

In contrast to the horizontal-field scanner geometry used in the clinical MRI systems described above, Pine et al. [20] presented a disk-shaped, vertical-field insert coil for the use with a 59 mT permanent-magnet vertical-field scanner. The combination of this geometry with a surface RF coil provides an improved flexibility with respect to the imaging region of the patient when compared to the reduction in accessible bore size for a solenoidal insert coil geometry currently used in horizontal-field MRI systems.

Technical comparisons

B_0 field stability and homogeneity

Most MRI image acquisitions are performed in the *k*-space and the phase of the NMR signal is essential for the image reconstruction process. Errors in the phase measurements in the order of half a degree or more lead to visible ghosting artefacts that degrade the image (see Figure 4). To mitigate this problem, field inhomogeneities are usually corrected by using spin echo sequences but this approach has limited results for time-varying

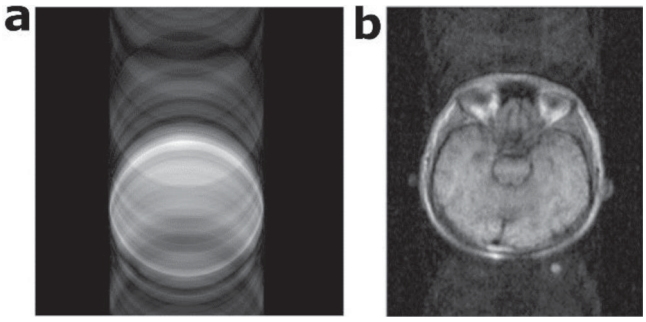

Figure 4. Small deviations of B_0 induce shifts in the signal phase that degrades the image producing ghosting artefacts e.g. (a) phantom image obtained from a B_0 insert coil [15] and (b) head scan obtained from a resistive whole-body magnet [25].

fluctuations. The average NMR phase from a simple spin-echo experiment can be modelled as follows:

$$\varphi(2\tau) = \gamma\left[\int_0^{\tau} B_0(t)dt - \int_{\tau}^{2\tau} B_0(t)dt\right] \quad (1)$$

where τ is the delay between the excitation and refocusing pulses, γ is the gyromagnetic ratio and $\varphi(2\tau)$ is the phase of the NMR signal when the echo forms. One can simplify the expression above by using a polynomial expansion of the field B_0:

$$\varphi(2\tau) = \gamma\left[\int_0^{\tau} \sum_{i=0}^{\infty} b_i t^i dt - \int_{\tau}^{2\tau} \sum_{i=0}^{\infty} b_i t^i dt\right] \quad (2)$$

where b_i are the decomposition coefficients of the B_0 series. This gives:

$$\varphi(2\tau) = \gamma \sum_{i=0}^{\infty} \frac{b_i}{i+1} \tau^{i+1}[2 - 2^{i+1}] \quad (3)$$

The terms of this series only cancel out for constant fields and dephasing increases with larger orders and with the echo time. Hence phase errors can only be corrected by better control of the magnetic field or by shortening the echo time, but the latter increases the acquisition bandwidth and lowers the SNR.

Permanent or superconducting magnets have stability time constant orders of magnitude larger than the echo time so they are not affected by this problem and any drift can be corrected by tracking the resonance frequency every few minutes. Fast temporal fluctuations of the magnetic field are mainly a problem when dealing with resistive magnets, either in isolation or in an insert system if the resistive coil is not disabled during image acquisition. In such systems, the field fluctuations that affect the phase of the NMR signal are due to imperfect control of the electric current by the magnet power supply. Yet resistive magnets are natural low-pass filters with a frequency f defined by their inductance L and resistance R:

$$f = R/2\pi L \quad (4)$$

It results that field stability is more easily achieved with large inductance and low resistance (which requires some compromises), however reducing the cut-off frequency of the magnet also reduces its response time for the field ramps and makes it more difficult to drive, requiring power supplies able to provide large voltages. Particular care is therefore necessary to design resistive magnets for FFC-MRI to balance these needs. As an example, ramp times are typically 1–10 ms long whereas echo times can reach 10–40 ms, hence a possible trade-off could be to set a cut-off frequency between 20 and 60 Hz.

For the insert system with the highest field offset reported above (500 mT obtained with 320 A, with and a cut-off frequency of $\sim$50 Hz [14]), the current fluctuations remaining during signal acquisition are typically producing NMR frequency fluctuations up to 200 Hz. To avoid such fluctuations during the acquisition phase, which uses the stable main field of the superconducting magnet, an ad-hoc strategy is to switch to a highly resistive state, which is equivalent to opening the coil circuit by disabling the amplifier [15]. Another approach is to switch the amplifier load between the insert coil and an inductance-matched dummy load using a fast high-power solid state switch [12].

Whole-body resistive FFC-MRI scanners present less problems and experimentation on the Aberdeen 0.2 T system showed fluctuations lower than 2 ppm (8 Hz proton Larmor frequency). It produces images with visible artefacts but these can be corrected by post-processing [25], where the background signal is minimised by finding the optimum phase correction for each k-space line.

Theses resistive magnets also produce heat that leads to field drift via thermal expansion, similar to what is observed with permanent magnets. This effect can reach 0.1% of the full field so it is of little concern for insert magnets but causes large field drifts in whole-body systems during the detection field. Correction techniques can easily be applied by scaling B_0 as the acquisition progresses, taking advantage of the long time constant associated with such thermal effects (40 min on the Aberdeen 0.2 T system). Yet this requires access to the data acquired during the scan.

Permanent magnets also present problems with field stability because of their temperature dependence. The dual FFC-MRI magnet at Aberdeen is based on ferrite and is thermally controlled but the resistive insert generates heat during field-cycled experiments. As a result, B_0 fluctuates over several kHz when acquiring field-cycled T_1 maps but the characteristic time of the drift is

very long compared with an acquisition so that one can make some corrections during the experiment, using one acquisition set to correct for the next one. Note that in this case the field correction cannot be done by adjusting B_0, but by adjusting the system frequency from the MRI console.

Signal-to-noise ratio

Signal-to-noise ratio (SNR) is a crucial parameter for MRI images: large SNR allows detecting with higher accuracy and improved spatial resolution, which are desirable for medical applications. SNR depends largely on the acquisition field strength [26], which limits the technology available for the detection of the NMR signal.

At NMR frequencies typically higher than 1 MHz (corresponding to 23 mT for ^{1}H), inductive detection can be used efficiently with mature technologies involving preamplifiers, acquisition electronics and radiofrequency coil designs. With such systems, the signal-to-noise ratio is summarised as:

$$\mathrm{SNR} = \gamma \mathrm{NPKC}\sqrt{T_{\mathrm{acq}}} \tag{5}$$

where γ is the gyromagnetic ratio, N is the number of nuclei within the imaged volume, P is the polarisation at equilibrium (which is proportional to the polarisation field under the Curie law), K provides the sensitivity of the RF detection coil (which is proportional to the acquisition field), C relates to the contrast due to relaxation and depends on the pulse sequence applied, and T_{acq} is the total acquisition time. As can be seen, in the choice of a strategy for FFC-MRI, the magnetic fields and their timing during the three distinct phases of polarisation, relaxation and acquisition interact in determining the achievable SNR. Separating each phase, SNR increases linearly with polarisation, motivating the use of high field or pre-polarising approaches when lower field FFC-MRI are used. Regarding the acquisition field, for biological tissues maintained at body temperature, an optimised RF detection setup would be in the sample-noise dominating regime, in which K is only dependent of the coil geometry and not on the acquisition frequency. However, in practice this regime is not always reached, when other noise sources dominate such as intrinsic RF coil noise, preamplifier noise and noise due to electromagnetic coupling with the environment. The limitation of noise performance depends on the acquisition field strength and RF coil size, with higher fields being more susceptible to patient noise while coil noise usually dominates at lower fields. Regarding the relaxation field that provides the image contrast, it is completely determined by the relaxation behaviour under the applied pulse sequence, with a trend to have shorter T_1 at lower fields, enabling to sensitise faster to this parameter. Finally, if an SNR is targeted for a given system, two basic imaging parameters can be adjusted to achieve it, the voxel size (to increase the number of nuclei N), and the available time the signal is actually acquired. In summary, an ideal system would benefit from high-field pre-polarisation, optimised acquisition field in the sample-noise dominating regime, and from the most relevant relaxation field to reveal field-dependant contrast.

However, in practice, experimental factors also impact SNR depending on the technology used. In particular, the heat dissipation in the resistive coil in FFC-MRI requires efficient cooling, and limitations of currently-available power-supply amplifiers lead to limited duty-cycles of the magnetic field. The most constrained systems in that matter are the resistive FFC-MRI magnets such as the one in Aberdeen which operates at a maximum of 50% duty ratio to allow the current amplifiers to cool down when operating at 0.2 T. Additionally, pre-polarisation at 0.2 T can only last up to 2 s so that tissues with long T_1 cannot be completely polarised, which decreases SNR accordingly. The cooling time is also lost in terms of acquisition time and increases the scan duration, typically by a factor 1.2–2. Insert systems also have restrictions imposed by their cooling systems but these mainly impact the magnet size because of the volume occupied by the cooling pipes.

RF coil setup

While a variety of commercial solutions exist for RF coils used in conventional MRI systems, FFC-MRI scanners present various non-standard features such that the RF coil has to be home-built. Design considerations differ according to the frequency regime and the RF coils designs vary between the insert and the whole-body systems even if in both systems the ratio of the wavelength to the cavity dimension is much larger than unity and the birdcage or saddle coil geometries are well-suited for the coil shape.

Insert magnet systems operating at 1.5 T or 3 T are characterised by resonant frequencies on the order of 100 MHz range and tight volume. An example of coil for such systems is presented in Figure 5 [27]: its diameter is set to fit tightly inside the insert bore of 40 mm diameter and the shield is very close to the coil during insertion, which causes large detuning when inserted inside the insert magnet. At high frequency the design of the inductive loop also needs to take into account the wavelength of the RF signal in the conductors. For MRI systems operating at 1.5 T, the proton NMR frequency is about 64 MHz and the corresponding wavelength in vacuum is 4.7 m. This number drops down to 2.8 m in

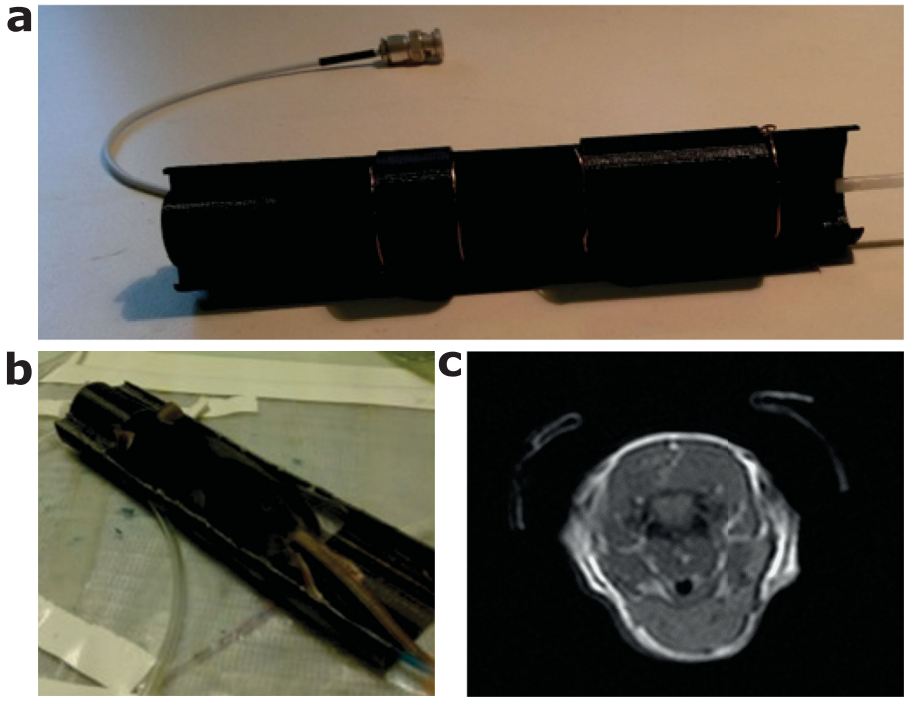

Figure 5. Specific RF coil design (a) and small animal bed adapted to gaseous anaesthesia (b) fitted to the tight available space due to the small bore size of the B_0 insert coil [27]. Exemplarily, an in vivo mouse image (axial slice at the neck level) obtained with the dedicated RF coil is shown in (c).

typical RG58 coaxial cables and is further reduced as B_0 increases. This requires particular care when placing lumped elements on large RF coils, such as used for human scans, and numerical simulations are required to validate the behaviour of the coil and avoid hot spots that could generate RF burns. Baluns are also needed at regular intervals along the transmission line to prevent current conduction along the cable shield, which could also result in burns and increases the signal noise, though these problems are not significant for animal-size systems.

Acquisition on the whole-body 0.2 T FFC-MRI scanner also requires custom RF coil design to adapt to low-frequencies, and this field strength is no longer used by MRI manufacturers. Such coils typically include large tuning capacitors, (typically hundreds or pF to several nF), large matching capacitors to adapt the load to the 50 Ohms transmission line (usually hundreds of pF), thick conductors to take advantage of the large skin depth (100 µm to accommodate a skin depth of about 20 µm) and large windings or multiple turns to increase the inductance. They also have some interesting benefits such as negligible dephasing with conductor length, since the wavelength at such frequencies is above 30 m, low power consumption from the RF power amplifier, Q factors typically between 100 and 400 depending on the geometry and low patient loading so that the Q factor remains high when the coil is used (coil noise regime). They also require very few baluns, if any, so the risk of RF burns remains small. An important improvement could come from the use of parallel imaging (PI) techniques [28] in FFC-MRI. PI is a routine method to accelerate image acquisition over a wide range of applications in conventional MRI, but this approach relies on the use of coil arrays and such detectors require additional components such as pin diodes for active decoupling and low input impedance preamplifiers for passive decoupling. The lack of readily available dedicated low-impedance preamplifiers at frequencies below 20 MHz makes coil arrays difficult to build at low frequencies for the moment. This is aggravated by the large inductors needed at low magnetic fields, which cannot be miniaturised into the currently existing high-field preamplifiers so that new designs must be created for applications at the MHz regime. Additionally, filtering elements such as present on the DC bias line of the PIN diodes are less efficient at low magnetic fields so that a trade-off must be found between the size and the signal loss of the coil array control boards. Developments in this field are currently ongoing in Aberdeen.

Eddy currents

FFC-MRI is prone to eddy currents resulting from the fast variations of the resistive coil inducing currents in all surrounding conductive materials. Their importance

consequently depends on the scanner design. Insert magnets tend to generate most eddy currents because of the large amount of conductive materials incorporated in the cryostats and support structures of superconductive magnets; eddy currents generated in liquid-He temperature structures such as radiation shields may be particularly problematic since the eddy current lifetime is prolonged due to high conductivity at low temperature. Insert magnet coils may need to be actively shielded in order to reduce the risk of quenching the main magnet. Eddy currents do appear significantly in dual-magnet FFC-MRI systems but a small delay before image acquisition ($\sim$1 ms) is usually sufficient to avoid artefacts, and no eddy currents have been observed so far in the Aberdeen team's purely-resistive FFC-MRI magnet, which can be explained by the absence of conductive surfaces around the magnet and the use of copper mesh for the RF shield.

Most effects have been reported in the case of insert coils into superconductive MRI systems used for dreMR imaging [12,14,15,29]. Typically, to characterise them, a ΔB_0 pulse of trapezoidal shape with defined ramps, flat top time and amplitude is applied. The induced eddy current field varies temporally and can be characterised by a mono-exponential (or even multi-exponential) decay. A comprehensive analysis of eddy current formation has been given by Hoelscher et al. in [29]. The main problem with induced eddy current fields is that they result in temporally varying offset in the Larmor frequency. This frequency offset gives rise to a shift of the field of view (FOV) along frequency and slice encoding axis causing substantial degradation of the dreMR image quality due to subtraction artefacts. A typical eddy current characterisation can be found in Figure 6(a). The influence of the shifted FOV on FFC-MRI images can be seen in Figure 6(b,c). To illustrate this problem, we consider a system with a maximum gradient strength of 45 mT/m acquiring over a slice thickness of 1 mm so that the maximum slice selection transmit bandwidth would be around 1.9 kHz. In such a situation the 380 Hz (peak) frequency shift induced by eddy currents as seen in Figure 6(c) dynamically shifts the FOV in the slice direction by up to 200 µm, a dynamic slice selection error of 20%. Similarly, such eddy currents would produce a shift of 180 µm within the plane of the image. This clearly indicates the need for a compensation of such effects for such preclinical systems.

Two strategies are then usable to compensate for these effects, the first one is to wait long enough to go below a predefined shift level, the other is to compensate based on an underlying calibrated linear model in prospective (through real-time RF modulation or compensation coils) or retrospective (through signal demodulation) ways, as the shifts are small enough to be restricted to the bandwidth of the RF setup. One prospective way to compensate eddy current effects, proposed by Hoelscher et al. [29], is to modulate the system reference frequency (based on the identified decay model) in such a way that the offset between system reference frequency and Larmor frequency is zero throughout the pulse sequence. In principle, this compensation can be implemented into any sequence type and does not require any additional hardware modifications. Another approach implemented by Harris et al. [12] is to apply an additional compensation field with a dedicated low-power Helmholtz coil counteracting the eddy current decay during image acquisition.

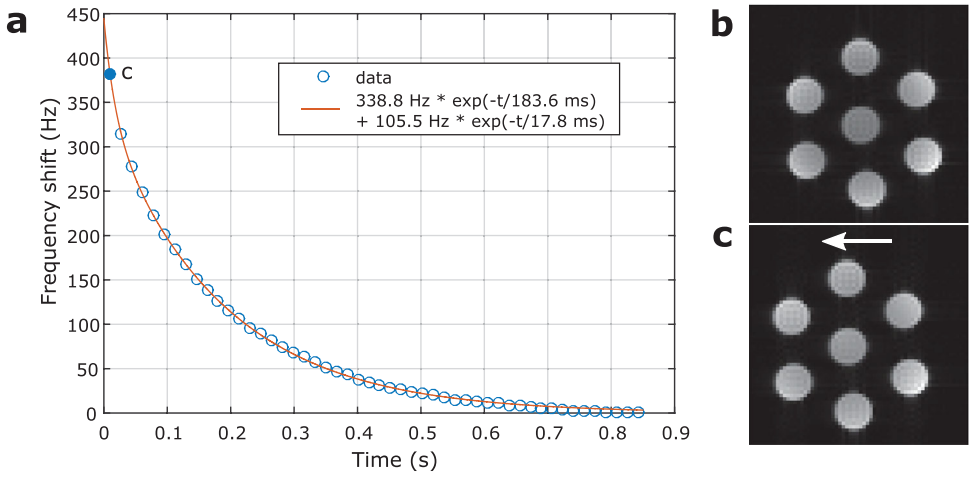

Figure 6. (a) Measured (blue circles) frequency shift induced by eddy currents in the FFC-MRI system for 3 T ($\Delta B_0 = 100$ mT, $T_{evol} = 300$ ms and ramp times of 1 ms) [15]. The red solid line represents a bi-exponential model fit. This frequency offset results in a shifted image (c) with respect to the reference image (b) without applied ΔB_0. The shifted image in (c) corresponds to the frequency offset in the first data point (filled circle) and clearly indicates the need to compensate for such eddy current effects.

Both approaches rely on an accurate eddy current characterisation and may be compromised by phase instabilities. It is important to note that the characterisation parameters are specific to the parameters of the ΔB_0 pulse such as amplitude, ramp times, flat top time and repetition time. For example, a compensation based on the parameters determined in Figure 6(a) is only valid for a ΔB_0 pulse with an amplitude of 100 mT, duration of 300 ms and ramp times of 1 ms. The repetition time (TR) has to be chosen to account for a sufficient eddy current decay before applying the next field-shift. In this example, a TR shorter than 900 ms would lead to an incorrect compensation as the eddy currents of the previous field-shift add to the eddy current field of the next one. Furthermore, the characterisation parameters may be altered slightly by a repositioning on the patient table between experiments. In practice, however, these problems can be overcome by performing a re-characterisation prior the actual experiment to account for different timing and field-shift parameters. Whereby, it is possible to account for other effects like a slightly altered coupling between the insert coil and the MRI system by a repositioning of the coil on the patient table between experiments.

Pulse sequences

Magnetisation-prepared spin-echo pulse sequences have been commonly used in FFC-MRI to determine R_1 dispersion maps (e.g. in [15,30,31]); this has been adopted as it corresponds to the gold-standard way to measure R_1. In the most general case, it comprises three phases between which the magnetic field B_0 is switched: polarisation, evolution and acquisition [11]. During the evolution phase the spin system undergoes relaxation imposed by the applied evolution field. Signal acquisition is always carried out at the same detection field strength and can either be the nominal B_0 of a permanent or superconducting magnet system, or at the maximum field for resistive magnets (coil noise dominance regime) to increase SNR. A pre-polarisation of the magnetisation is not necessarily required in the high SNR regime and therefore the polarisation field is equal to the detection field. This scheme has to be repeated in the usual manner for the acquisition of the whole k-space.

One important limitation of FFC in the design of pulse sequences comes from the detection technology. The use of tuned transmit and receive coils imposes the use of the corresponding field for detection and as a consequence only the detection field allows modifying the spin system by RF pulses, or detecting the NMR signal. This forbids the use of speed-up strategies such as parallel slice acquisitions, at least during the evolution field. FFC measurements are also iterative: R_1 maps are generated for each evolution field by acquiring a series of images with varying evolution times. As an example, a 128×128 image with 12 sec repetition time, and 2 evolution fields and 5 evolution times would provide a quantitative $\Delta R_1/\Delta B_0$ map in 4 h and 16 min, which is definitely not practical.

Depending on the application, qualitative $\Delta R_1/\Delta B_0$-weighted images (e.g. dreMR image contrast) can be acquired, as illustrated in Figure 7(b), in such case the overall measurement time can be reduced by acquiring only two images needed for image subtraction. In the above example this would lead to a measurement time of 51 min, which is achievable for in vivo scans but not practical for clinical use. It is therefore crucial in FFC-MRI to speed up the measurement procedure under consideration of particular hardware restrictions and without significantly compromising the SNR.

FFC-MRI offers two ways to do so, either by speeding-up k-space acquisition strategies or by exploiting the data redundancy in the NMRD profile. For the latter, Broche et al. [21] proposed a multi-field two-point method to estimate R_1 for different evolution fields, reducing the number of images to one image per evolution field and an additional reference image taken at the detection field. This approach provides reasonably accurate R_1 values in less time and is valid for relatively linear regions in the NMRD profile. To speed up k-space acquisition in the context of FFC-MRI, several strategies have been followed successfully, such as faster imaging modules like RARE (Rapid Acquisition with Refocused Echoes) [32]. In contrast to conventional spin echo sequences, in RARE imaging multiple lines of k-space are acquired within one TR interval instead of only one. Echo train lengths of up to 4 were used in studies by Ross et al. [30] and Araya et al. [31] without image degradation. This speed up by a factor of 4 reduces the acquisition time per image in our example from approximately 25 min to a reasonable 6 min. Furthermore, the use of steady-state sequences like fast low-angle shot (FLASH) [33] or IR-Look-Locker [34,35] may be considered in conjunction with field-cycling. In the line of the adaptation of fast MRI pulse sequence with R_1 contrast, Chanet et al. [36] provided a theoretical derivation and analysis of the FLASH steady-state signal equation modified for field-cycling. Such sequences are usually used with short TRs, which, on the one hand, may reduce the acquisition time significantly but on the other hand poses high demands on the FFC hardware. In particular, TR could be limited by eddy current effects, ramp times and/or duty-cycle of the field shifts.

The choice of acquisition schemes is reduced in the Aberdeen team's resistive FFC-MRI scanner because of the limited duty-cycle ratio of the scanner. As mentioned

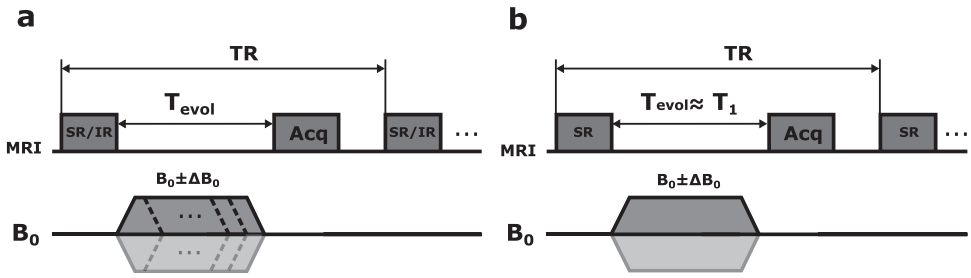

Figure 7. Comparison between FFC-MRI pulse sequences used for (a) quantitative $\Delta R_1/\Delta B_0$ mapping and (b) qualitative R_1 dispersion imaging in the case of dreMR imaging. In (a) R_1 mapping is performed at different fields by acquiring a series of images with various T_{evol} increasing the overall measurement time by the total number of needed T_{evol} and evolution fields. For example, a series of 10 images is needed for 2 evolution fields ($B_0 \pm \Delta B_0$) and 5 T_{evol} per field. In comparison, for dreMR imaging in (b) only one T_{evol} is needed, which is chosen in the order of T_1 to maximise SNR, therefore the overall measurement time can be reduced to the acquisition time of 2 images needed for image subtraction.

earlier, this scanner may overheat if driven continuously and a 20–50% duty cycle must be observed to avoid problems so that steady-state approaches are difficult to develop. Additionally, the field temporal stability is relatively poor and the signal phase fluctuates randomly with a typical decorrelation time of 15 ms, making CPMG or other similar techniques inefficient. This also prevents averaging the complex signal since the random phase error tends to cancel the signal out.

Potential applications

Contrast-to-noise ratio

While SNR is important to characterise an MRI system, Contrast-to-Noise Ratio (CNR) is what ultimately determines the usefulness of an image. We define CNR here as how much the SNR varies with respect to an underlying physical parameter of interest. In MRI, the sources of contrast mainly rely on T_1 and T_2 at fixed B_0 field. In FFC-MRI, the source of contrast up to now has mainly been based on T_1 dispersion. For instance, considering a polynomial expansion of R_1 around the magnetic field B_0 as $R_1 = R_{10} + \beta^* \Delta B_0$, where R_{10} is the relaxation rate at the field B_0, and β the slope of the dispersion profile, one possible dreMR-related CNR could be:

$$\mathrm{CNR} = \frac{\Delta \mathrm{SNR}}{\Delta B_0} \tag{6}$$

Indicating that dreMR contrast is maximised when the slope of the signal is the largest. Considering an inversion-recovery sequence, where the signal equation is proportional to $1–2^*\exp(-R_1{}^*T_{evol})$ with T_{evol} the evolution time, in first approximation, the CNR, corrected from thermal equilibrium will vary as a function of $\beta^* T_{evol}$. Reciprocally, the CNR as a function of β is linked to the product $\Delta B_0{}^* T_{evol}$, such that larger field offsets and longer application times are more sensitive.

Besides T_1, T_2 dispersion may also be of interest. However, it is technically difficult to maintain phase coherence while switching the magnetic field. Initial work has been done to access R_2 dispersion profiles in FFC-MRI systems [37], with the major target of endogenous ferritin imaging [38] that, as a major component of iron metabolism, may represent a biomarker of neurodegenerative diseases.

It is important to consider that T_1 varies significantly between different magnetic fields. This effect is more pronounced in tissues that disperse strongly, such as cartilage or muscle, and less so in fatty tissues or brain. Other effects may influence the contrast such as quadrupolar relaxation, as explained later. Therefore, CNR using FFC-MRI varies depending on the field strength that can be accessed, and therefore on the technology employed, and its evaluation and benefits for biomedical applications are widely unexplored. Here we present some contrast mechanisms accessible by the FFC-MRI systems presented here.

Quadrupole peaks due to ^{14}N – ^{1}H cross-relaxation

The presence of cross-linked proteins in tissues may result in local increases in the R_1 relaxation rate in the dispersion curves of protons at particular magnetic fields, around ^{1}H Larmor frequencies of 600 kHz, 2.2 MHz and 2.8 MHz, respectively. This quadrupole cross-relaxation effect has been first reported in living biological tissues by Kimmich et al. [39] and is now relatively well understood as being due to a transfer of magnetisation between water protons and the ^{14}N nuclei, probably from amine and/or amide groups of protein backbones, even though the transfer mechanism from the protein proton to the bulk water is still a topic of debate. Nevertheless, efficient models exist that allow predicting this so-called Quadrupole Enhanced Relaxation (QRE) for an arbitrary quadrupole spin number [40].

QRE from ^{14}N is an interesting source of contrast since it is naturally found in vivo and it directly informs on the presence of immobilised proteins. Experiments on cross-linked albumin [41] or the fibrin system [42] showed that the amplitude of the peak is directly proportional to the concentration of the protein responsible for the relaxation enhancement, which makes this a quantitative biomarker. However, experimentation on biological tissues have so far only found the same pattern of peaks, so this signal does not discriminate between different sources and does not inform on the nature of the protein responsible for it. Another important aspect of the ^{14}N quadrupole peaks is that they appear at relatively low magnetic fields so that they are not accessible by high-field insert technologies such as those used for dreMR.

Experiments with FFC-MRI scanner and FFC-NMR relaxometer have shown interesting applications for the ^{14}N quadrupole signals in muscle atrophy [43] and osteoarthritis [10,44]. In both pathologies, the amplitude of the peaks informs on the protein structures, which relates to the pathology.

Dispersive contrast agents for FFC-MRI

The fact that some MRI contrast agents show a strong dependence of R_1 upon the magnetic field can be exploited by FFC-MRI [45–47]. The idea is to acquire one image (or even a relaxometric R_1 map) for an evolution field where the probe shows a high relaxivity, and another one with an evolution field corresponding to a low relaxivity. In this way one can obtain image contrast based on the slope dR_1/dB_0 of the contrast agent's NMRD profile. In the low field range, FFC-MRI mainly relies on the large endogenous R_1 dispersion of biological tissues, which can show the aforementioned quadrupole peaks due to ^{14}N – ^{1}H cross-relaxation, but can also benefit from the use of exogenous contrast agents. O'Hogain et al. [48] investigated the use of liposomes encapsulating paramagnetic Mn[II] ions as a tailored FFC-MRI contrast agent for low field applications. This probe shows a large difference in relaxivity values between 5 and 60 mT, whereas the reference sample displays almost no change in relaxivities over the same field range. In the high field range (above 0.5 T), R_1 dispersion of tissue becomes relatively invariant as several NMRD studies have emphasised [49,50]. There is a relatively simple decrease of R_1 with field above 0.5 T, with proposed descriptions involving a macromolecular-based power law and a logarithmic term involving the restricted diffusive exploration of the macromolecular interfaces [51]. Endogenous R_1 dispersion properties can thus be characterised by a small number of parameters, including the slope of the dispersion profile around the central B_0 value, providing contrast sensitive to the macromolecular content, although there still are no in vivo studies exploiting this aspect with FFC-MRI.

To date, FFC-MRI for typical clinical-system field strengths (1.5 or 3.0 T) mainly relies on the use of contrast agents with a strong magnetic field dependency in the corresponding field-cycling range. Alford et al. [52] were the first to introduce the dreMR method for *in vitro* differentiation between the bound and unbound state of gadofosveset at 1.5 T. This probe exhibits a strong R_1 dispersion upon activation by binding to large molecules such as serum albumin but shows weak R_1 dispersion in the unbound state. Araya et al. [12] conducted *in vivo* experiments with mice demonstrating an unambiguous localisation of gadofosveset activated by protein binding. Hoelscher et al. [13] extended these results by quantitative measurements of concentration using the dispersive contrast agent Gadofluorine M. Furthermore, it was shown by Bödenler et al. [15] that iron oxide magnetic nanoparticles (IOMNPs) are suitable for in-vitro FFC-MRI studies up to 3 T. The corresponding NMRD profiles, as illustrated in Figure 8(a), exhibit a sufficiently high $\Delta R_1/\Delta B_0$ to perform dreMR imaging or relaxometric mapping in the field-cycling range of 2.89 T $\pm$ 0.1 T (Figure 8(b)).

All these results demonstrate the potential of FFC-MRI in the field of contrast agents, to improve the sensitivity and specificity of contrast agent detection over a wide range of field strengths. Although approximately 40% of clinical MRI exams employ Gadolinium-based CAs [53], the availability of clinical approved CAs suitable for FFC-MRI is rather limited. The aforementioned gadofosveset was designed as blood pool agent for contrast-enhanced MR angiography and is approved for a clinical use [54]. This agent shows favourable dispersive properties in the clinical field range between 1.5 T and 3 T, but the manufacturer discontinued the production in 2017 [55]. Iron oxide nanoparticles also show dispersive properties in the clinical field range. For example, ferumoxytol is approved by the United States Food and Drug Administration (FDA) for treatment of iron deficiency anaemia in adult patients and its off-label use as MRI contrast agent has rapidly grown [56,57]. Over the years, significant effort has gone into the development of new MRI contrast agents but sophisticated toxicology and pharmaceutical investigations are necessary to take the step from preclinical development to approval for clinical use.

One important means to determine the suitability of contrast agents for FFC-MRI is the measurement of the ^{1}H R_1 NMRD profile by FFC-NMR relaxometry. For paramagnetic systems the shape of the NMRD profile

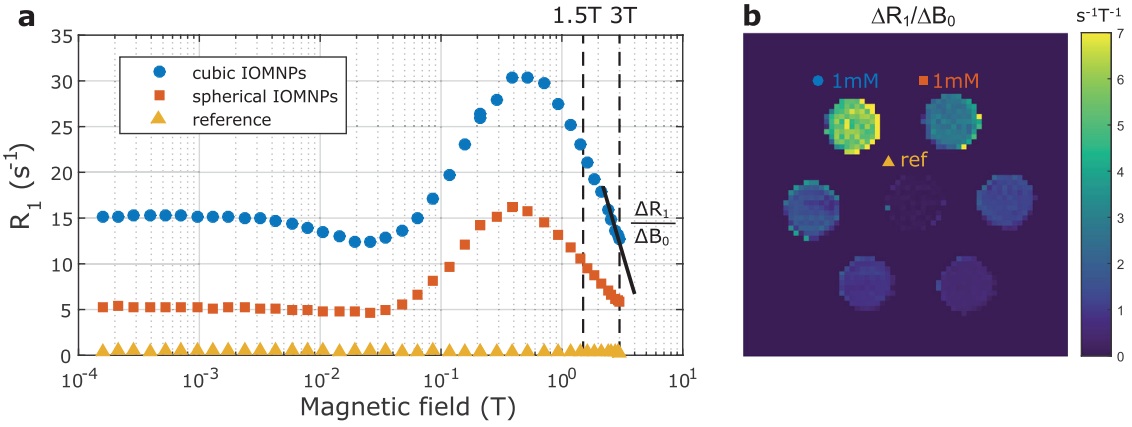

Figure 8. (a) ^{1}H R_1 NMRD profiles of cubic- and spherical-shaped IOMNPs with 1 mM concentration, compared to a reference NMRD profile of pure hexane. The IOMNPs show a significantly high R_1 dispersion in the high field range to perform FFC-MRI studies up to 3 T. Based on the slope in the respective field-cycling range, a $\Delta R_1/\Delta B_0$ image can be obtained by subtracting two R_1 maps acquired at different fields. In particular, (b) shows a $\Delta R_1/\Delta B_0$ map obtained for an FFC range of 2.89 T $\pm$ 0.1 T using samples containing a twofold serial dilution series (top down, starting with 1 mM) of cubic (left) and spherical (right) IOMNPs. Samples with dispersive IOMNPs show high $\Delta R_1/\Delta B_0$ in contrast to the non-dispersive reference sample (centre). [15]

is influenced by various parameters such as the water exchange rate, coordination number, rotational correlation time and electron spin relaxation [45]. As already shown with the protein-binding gadofosveset, the most promising for FFC-MRI are slowly tumbling systems where the reorientational correlation time τ_R becomes long. This leads to a relaxivity peak located between 20 and 80 MHz followed by a steep downward slope which can be exploited by a clinical FFC range. In future, it may be possible to design contrast agents specific for FFC-MRI by aiming for extremely high $\Delta r_1/\Delta B_0$ in the activated state and almost no $\Delta r_1/\Delta B_0$ in the inactivated state.

Potential frequency-selective contrast agents for FFC-MRI

A promising alternative to the currently used contrast agents for FFC-MRI is the design of frequency-selective molecular probes based on Quadrupole Relaxation Enhancement (QRE). The idea is to utilise QRE between water protons and exogenous quadrupole nuclei, similar to the aforementioned interaction between endogenous ^{1}H and ^{14}N in the amide groups of proteins at low field strengths. QRE becomes effective if the ^{1}H Larmor frequency matches one of the frequencies with high transition probability of the quadrupole nuclei, a condition which depends on the Quadrupole Coupling Constant Q_{cc}, the asymmetry parameter η and the Zeeman splitting [58]. Q_{cc} and η are the main parameters describing the frequency positions of the nuclear quadrupole spin transitions of a QRE active molecule. Consequently, QRE based contrast agents show a frequency-selective nature, similar to the quadrupole peaks due to ^{14}N-^{1}H cross-relaxation.

For instance, several compounds containing high spin quadrupole nuclei such as ^{209}Bi show very characteristic QRE patterns in the field range between 0.5 T and 3 T, as was recently shown by Kruk et al. [59] in NMRD studies of solid powder samples. For the envisaged aim of an exogenous QRE contrast agent, one would require, in a next step, to show QRE in the liquid state by grafting these core compounds onto nanoparticles and dissolve them in an aqueous solution. The relaxation dynamics of QRE in the liquid state can be simulated by the stochastic Liouville approach [58,60,61]. As an example, a simulated NMRD profile for a possible QRE contrast agent is displayed in Figure 9 for tris(2-methoxyphenyl)bismuthane. Several QRE peaks emerging up to 3 T indicate the potential to exploit this frequency-selective nature with FFC-MRI to enhance image contrast. Moreover, the overlay with FFC ranges of currently available FFC-MRI systems clearly shows the benefit of a wide variety of cycling ranges as it is completely unexplored at which field strength such compounds lead to the best image contrast.

Another interesting consideration is that the Q_{cc} is sensitive to structural changes in the chemical surrounding of the quadrupole nuclei. It is possible to tune the quadrupole transition frequency, and therefore the QRE effect, by attaching different substituents to the core compound. Recently, Gösweiner et al. [62] showed the tuning possibilities of the resonance condition for various Bi-aryl compounds. Although current research is focusing on ^{209}Bi as core compound, it is also conceivable to use other quadrupole nuclei to design QRE based contrast agents specific for a FFC range of choice.

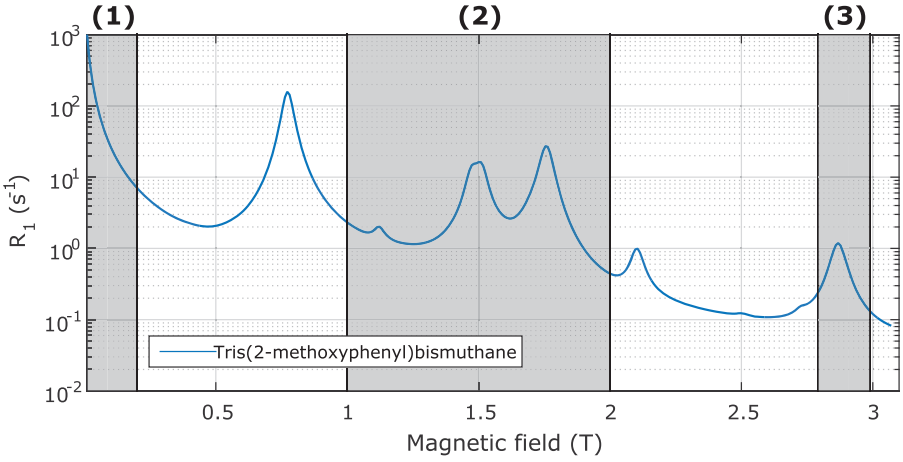

Figure 9. ^{1}H R_1 NMRD profile of a potential QRE based contrast agent simulated with the stochastic Liouville approach for a rotating, coupled system ^{209}Bi-^{1}H with a rotational correlation time of 300 ns, inter-nucleus distance of 2 Å, Q_{cc} of 715 MHz and $\eta = 0$ (parameters taken from [62]). The grey overlay illustrates achievable FFC ranges of different FFC-MRI systems: (1) up to 0.2 T [19] (2) 1.5 T $\pm$ 0.5 T [14] and (3) 2.89 T $\pm$ 0.1 T [15].

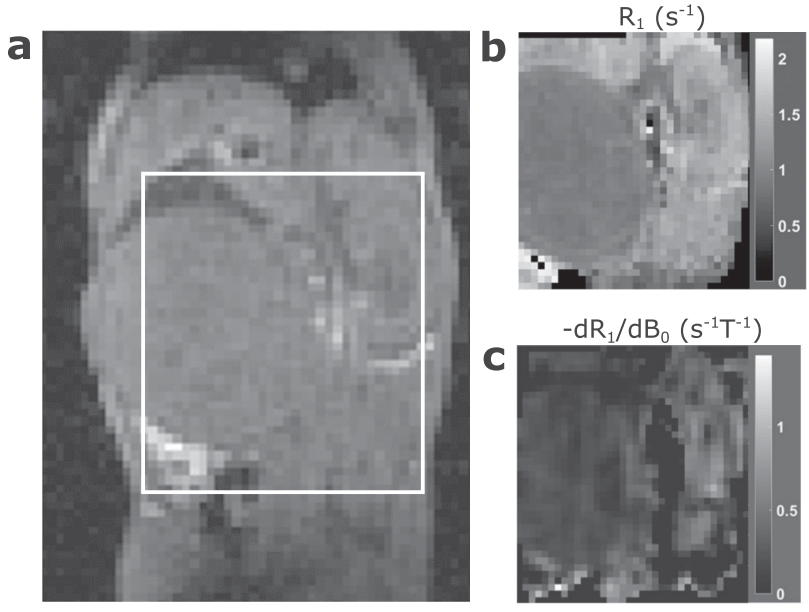

Figure 10. In vivo FFC-MRI measurements in a kidney tumour mouse model obtained from the preclinical insert system operating at 1.5 T $\pm$ 0.5 T [63]. (a) Standard spin-echo T_1-weighted image (0.5 mm isotropic in-plane and 2.5 mm through-plane resolution, acquisition time per image is $\sim$5 min) of the abdomen of a mouse acquired at 1.5 T. (b) R_1 map at 1.5 T corresponding to the white square in (a). (c) Corresponding dispersion ($-dR_1/dB_0$) map calculated for three different field strengths of 1.34 T, 1.5 T and 1.66 T. The tumour displays lower R_1 and $-dR_1/dB_0$ than the medulla and kidney.

FFC-MRI on biological tissues

Thanks to the recent technological improvements of FFC-MRI systems leading to exploitable image quality, initial in-vivo biomedical imaging applications are emerging. Figures 10 and 11 display typical images obtained with clinical and preclinical systems with anatomical targets such as brain, musculoskeletal and abdominal regions, and current pathological targets that mostly focused on cancer. These examples illustrate the excellent image quality that FFC-MRI can provide, and initial biomedical evaluation of the translation from FFC-NMR to FFC-MRI. In the future, it is expected that the successful biological applications of FFC-NMR [64] will be translated to FFC-MRI, leading to new imaging biomarkers of diseases that still remain to be validated and compared to the already rich contrast available on conventional fixed-field MRI systems.

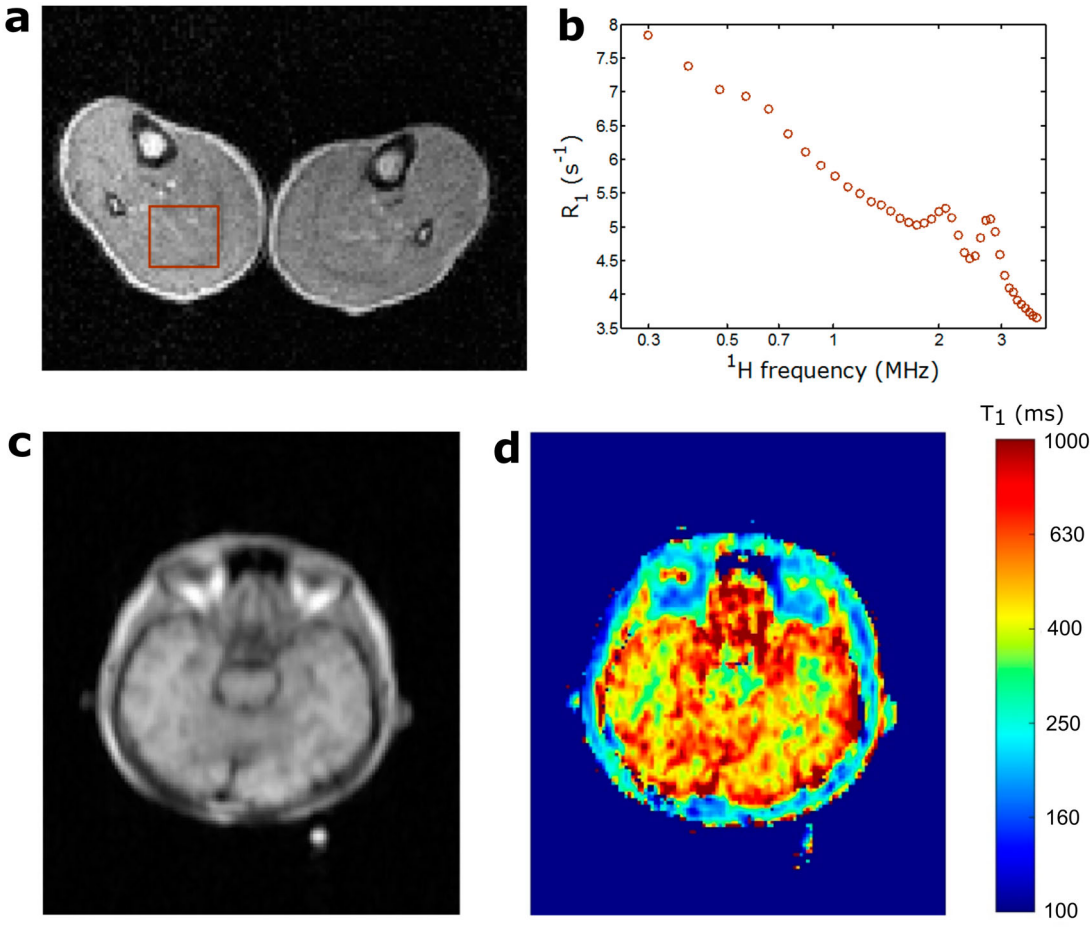

Figure 11. Data obtained from whole-body FFC-MRI scanners (from [43]). (a) 1 cm-thick section of thighs of a healthy volunteer, obtained at 59 mT from the dual-magnet system presented in [18]. Relaxometry was performed using FC-PRESS over a volume of interest to provide dispersion curves (b). (c) Spin echo image from a healthy volunteer's head obtained at 0.2 T from the resistive magnet presented in [19] (32 ms echo time, polarisation at 0.2 T for 0.3 s, 6 mm slice thickness, 2.3 mm in-plane resolution, 0.3 s recycle delay at Earth field). The T_1 map at that field is shown in (d); it clearly shows the difference between grey matter, white matter, and fatty tissues.

Conclusions

Fast Field-Cycling provides a wealth of information at a molecular level and pioneer works on FFC-MRI show promising results, but also additional technical complexity. The compromises that have to be made to develop FFC-MRI scanners have to balance field strength, B_0 bandwidth, scanner size, field stability and scan time. The technologies presented in this paper show several approaches that allow exploring different regions of the magnetic field strength and present different advantages and drawbacks.

Extending the measurement of the dispersion curve towards low magnetic fields is more easily performed using a single electromagnet, at the cost of degraded field stability. This may be mitigated by using detection methods at very low field and has the added benefit to provide near-immunity against ferromagnetic elements, at the cost of SNR and possible additional complexity. Fields ranging between several mT and 0.5 T can be probed using a combination of permanent and resistive magnets. This prevents field fluctuations during readout but limits the lowest field attainable. T_1 dispersions at high magnetic fields can be measured using a combination of resistive insert coils and superconducting magnets. This provides high SNR and resolution, at the cost of lower usable volume and lower B_0 bandwidth.

These various technical solutions allow covering a wide range of the magnetic field spectrum and collaborative work is now possible to explore T_1 dispersion contrast mechanisms over 5 decades of B_0, from 20 µT to 3 T. This opens new research avenues for the discovery of biomarkers as well as to better understand pathological processes at the molecular level. In conclusion, FFC-MRI is emerging as a powerful research tool readily available, and future developments may enable exploring its large potential for biomedical applications.

Disclosure statement

No potential conflict of interest was reported by the authors.

Funding

This article is based upon work from COST Action CA15209, supported by COST (European Cooperation in Science and Technology). M. Bödenler, C. Gösweiner and H. Scharfetter acknowledge the financial support by the European Commission in the frame of the H2020 Future and Emerging Technologies (FET-open) under grant agreement 665172, project 'CONQUER'. L. de Rochefort acknowledges the France Life Imaging network (Grant ANR-11-INBS-0006) that partially funded the small animal FFC-MRI system. D.J. Lurie, L.M. Broche and P.J. Ross acknowledge funding from the European Union's H2020 research and innovation programme under grant agreement No 668119, project 'IDentIFY'.

ORCID

Christian Gösweiner http://orcid.org/0000-0003-4453-9385

References

[1] R.W. Brown, Y.C.N. Cheng, E.M. Haacke, M.R. Thompson and R. Venkatesan, Magnetic Resonance Imaging: Physical Principles and Sequence Design: Second Edition (Wiley Blackwell, 2014).
[2] F. Noack, Prog. Nucl. Magn. Reson. Spectrosc. **18**, 171 (1986).
[3] R. Kimmich and E. Anoardo, Prog. Nucl. Magn. Reson. Spectrosc. **44**, 257 (2004).
[4] D. Kruk, A. Herrmann and E.A. Rössler, Prog. Nucl. Magn. Reson. Spectrosc. **63**, 33 (2012).
[5] F. Barberon, J.P. Korb, D. Petit, V. Morin and E. Bermejo, Phys. Rev. Lett. **90**, 4 (2003).
[6] R.M. Steele, J.P. Korb, G. Ferrante and S. Bubici, Magn. Reson. Chem. **54**, 502 (2016).
[7] Y. Wang, H. Cooperman, V.M. Rao, M. Nino-Murcia, S.H. Koenig and R.D. Brown, Magn. Reson. Imaging **2**, 235 (1984).
[8] S.H. Koenig and R.D. Brown, Prog. Nucl. Magn. Reson. Spectrosc. **22**, 487 (1990).
[9] E. Rössler, C. Mattea and S. Stapf, J. Magn. Reson. **251**, 43 (2015).
[10] L.M. Broche, G.P. Ashcroft and D.J. Lurie, Magn. Reson. Med. **68**, 358 (2012).
[11] D.J. Lurie, S. Aime, S. Baroni, N.A. Booth, L.M. Broche, C.H. Choi, G.R. Davies, S. Ismail, D. O'Hógáin and K.J. Pine, Comptes Rendus Phys. **11**, 136 (2010).
[12] C.T. Harris, W.B. Handler, Y. Araya, F. Martinez-Santiesteban, J.K. Alford, B. Dalrymple, F. Van Sas, B.A. Chronik and T.J. Scholl, Magn. Reson. Med. **72**, 1182 (2014).
[13] U.C. Hoelscher, S. Lother, F. Fidler, M. Blaimer and P. Jakob, Magn. Reson. Mater. Physics, Biol. Med. **25**, 223 (2012).
[14] L. de Rochefort, E. Lee, M. Polello, L. Durrasse, G. Ferrante and B.K. Rutt, Proc. Intl. Soc. Mag. Reson. Med. **20** (2012).
[15] M. Bödenler, M. Basini, M.F. Casula, E. Umut, C. Gösweiner, A. Petrovic, D. Kruk and H. Scharfetter, J. Magn. Reson. **290**, 68 (2018).
[16] G. Ferrante and S. Sykora, Adv. Inorg. Chem. **57**, 405 (2005).
[17] M. Espy, A. Matlashov and P. Volegov, J. Magn. Reson. **229**, 127 (2013).
[18] D.J. Lurie, M.A. Foster, D. Yeung and J.M.S. Hutchison, Phys. Med. Biol. **43**, 1877 (1998).
[19] P.J. Ross, L.M. Broche, G.R. Davies and D.J. Lurie, Proc. Intl. Soc. Mag. Reson. Med. **25** (2017).
[20] K.J. Pine, F. Goldie and D.J. Lurie, Magn. Reson. Med. **72**, 1492 (2014).
[21] L.M. Broche, P. James Ross, K.J. Pine and D.J. Lurie, J. Magn. Reson. **238**, 44 (2014).
[22] J.K. Alford, T.J. Scholl, W.B. Handler and B.A. Chronik, Concepts Magn. Reson. Part B Magn. Reson. Eng. **35B**, 1 (2009).
[23] C.T. Harris, J.K. Alford, W.B. Handler, T.J. Scholl and B.A. Chronik, Proc. Intl. Soc. Mag. Reson. Med. **18** (2010).
[24] C.T. Harris, W.B. Handler, T.J. Scholl and B.A. Chronik, Proc. Intl. Soc. Mag. Reson. Med. **19** (2011).
[25] L.M. Broche, P.J. Ross, G.R. Davies and D.J. Lurie, Magn. Reson. Imaging **44**, 55 (2017).
[26] D.I. Hoult and R.E. Richards, J. Magn. Reson. **213**, 329 (2011).
[27] G. Guillot, L. Jourdain, N. Chanet, R.-M. Dubuisson, M. Poirier-Quinot and L. de Rochefort, Magn. Reson. Mater. Physics, Biol. Med. **30**, 316 (2017).
[28] D.J. Larkman and R.G. Nunes, Phys. Med. Biol. **52**, R15 (2007).
[29] U.C. Hoelscher and P.M. Jakob, Magn. Reson. Mater. Physics, Biol. Med. **26**, 249 (2013).
[30] P.J. Ross, L.M. Broche and D.J. Lurie, Magn. Reson. Med. **73**, 1120 (2015).
[31] Y.T. Araya, F. Martínez-Santiesteban, W.B. Handler, C.T. Harris, B.A. Chronik and T.J. Scholl, NMR Biomed. **30**, e3789 (2017).
[32] J. Hennig, A. Nauerth and H. Friedburg, Magn. Reson. Med. **3**, 823 (1986).
[33] A. Haase, J. Frahm, D. Matthaei, W. Hanicke and K.-D. Merboldt, J. Magn. Reson. **67**, 258 (1986).
[34] D.C. Look and D.R. Locker, Rev. Sci. Instrum. **41**, 250 (1970).
[35] G. Brix, L.R. Schad, M. Deimling and W.J. Lorenz, Magn. Reson. Imaging **8**, 351 (1990).
[36] N. Chanet and L. de Rochefort, Proc. Intl. Soc. Mag. Reson. Med. **24** (2016).
[37] N. Chanet, G. Guillot and L. de Rochefort, Proc. Intl. Soc. Mag. Reson. Med. **25** (2017).
[38] J. Vymazal, R.A. Brooks, O. Zak, C. Mcrill, C. Shen and D.G. Chiro, Magn. Reson. Med. **27**, 368 (1992).
[39] R. Kimmich, W. Nusser and F. Winter, Phys. Med. Biol. **29**, 593 (1984).
[40] P.H. Fries and E. Belorizky, J. Chem. Phys. **143**, 44202 (2015).
[41] X. Jiao and R.G. Bryant, Magn. Reson. Med. **35**, 159 (1996).
[42] L.M. Broche, S.R. Ismail, N.A. Booth and D.J. Lurie, Magn. Reson. Med. **67**, 1453 (2011).
[43] K.J. Pine, G.R. Davies and D.J. Lurie, Magn. Reson. Med. **63**, 1698 (2010).

[44] E. Rössler, C. Mattea and S. Stapf, Magn. Reson. Med. **73**, 2005 (2014).
[45] S. Aime, M. Botta, D. Esteban-Gómez and C. Platas-Iglesias, Mol. Phys. **8976**, 1 (2018).
[46] J.R. Morrow and É. Tóth, Inorg. Chem. **56**, 6029 (2017).
[47] M.W. Rotz, K.S.B. Culver, G. Parigi, K.W. Macrenaris, C. Luchinat, T.W. Odom and T.J. Meade, ACS Nano **9**, 3385 (2015).
[48] D. Ó Hógáin, G.R. Davies, S. Baroni, S. Aime and D.J. Lurie, Phys. Med. Biol. **56**, 105 (2011).
[49] P.A. Bottomley, T.H. Foster, R.E. Argersinger and L.M. Pfeifer, Med. Phys. **11**, 425 (1984).
[50] S.F. Akber, Physiol. Chem. Phys. Med. NMR **28**, 205 (1996).
[51] G. Diakova, J.-P. Korb and R.G. Bryant, Magn. Reson. Med. **68**, 272 (2012).
[52] J.K. Alford, B.K. Rutt, T.J. Scholl, W.B. Handler and B.A. Chronik, Magn. Reson. Med. **61**, 796 (2009).
[53] Z. Zhou and Z.-R. Lu, Wiley Interdiscip. Rev. Nanomed. Nanobiotechnol. **5**, 1 (2013).
[54] P. Caravan, N.J. Cloutier, M.T. Greenfield, S.A. McDermid, S.U. Dunham, J.W.M. Bulte, C. Amedio John, R.J. Looby, R.M. Supkowski, D.W. Horrocks William, T.J. McMurry and R.B. Lauffer, J. Am. Chem. Soc. **124**, 3152 (2002).
[55] D.J. Bell and M.A. Morgan, (2018). https://radiopaedia.org/articles/gadofosveset-trisodium-1.
[56] G.B. Toth, C.G. Varallyay, A. Horvath, M.R. Bashir, P.L. Choyke, H.E. Daldrup-Link, E. Dosa, J.P. Finn, S. Gahramanov, M. Harisinghani, I. Macdougall, A. Neuwelt, S.S. Vasanawala, P. Ambady, R. Barajas, J.S. Cetas, J. Ciporen, T.J. DeLoughery, N.D. Doolittle, R. Fu, J. Grinstead, A.R. Guimaraes, B.E. Hamilton, X. Li, H.L. McConnell, L.L. Muldoon, G. Nesbit, J.P. Netto, D. Petterson, W.D. Rooney, D. Schwartz, L. Szidonya and E.A. Neuwelt, Kidney Int. **92**, 47 (2017).
[57] S.S. Vasanawala, K. Nguyen, M.D. Hope, M.D. Bridges, T.A. Hope, S.B. Reeder and M.R. Bashir, Magn. Reson. Med. **75**, 2107 (2016).
[58] D. Kruk, A. Kubica, W. Masierak, A.F. Privalov, M. Wojciechowski and W. Medycki, Solid State Nucl. Magn. Reson. **40**, 114 (2011).
[59] D. Kruk, E. Umut, E. Masiewicz, C. Sampl, R. Fischer, S. Spirk, C. Goesweiner and H. Scharfetter, Phys. Chem. Chem. Phys. **20**, 12710 (2018).
[60] R. Kubo, J. Math. Phys. **4**, 174 (1963).
[61] P.-O. Westlund and H. Wennerstrom, J. Magn. Reson. **63**, 280 (1985).
[62] C. Gösweiner, P. Lantto, R. Fischer, C. Sampl, E. Umut, P. Westlund, D. Kruk, M. Bödenler, S. Spirk, and A. Petrovic, Phys. Rev. X **8**, 021076 (2018).
[63] N. Chanet, G. Guillot, I. Leguerney, R.-M. Dubuisson, C. Sebrié, A. Ingels, N. Assoun, E. Daudigeos-Dubus, B. Geoerger, N. Lassau, L. Broche and L. de Rochefort, Proc. Intl. Soc. Mag. Reson. Med. **26** (2018).
[64] M.R. Ruggiero, S. Baroni, S. Pezzana, G. Ferrante, S.G. Crich, and S. Aime, Angew. Chem. **130** (25), 7590 (2018).